

# 3D-OSEM iterative image reconstruction for high-resolution PET using precalculated system matrix

Juan E. Ortuño\*, Pedro Guerra-Gutiérrez, José L. Rubio, George Kontaxakis, Andrés Santos

*Department of Electronic Engineering, Biomedical Image Technology, Universidad Politécnica de Madrid, 28040 Madrid, Spain*

Available online 15 September 2006

## Abstract

An efficient iterative image reconstruction methodology is presented, adapted to high-resolution flat-head 3D positron emission tomography cameras. It is based on the ordered subsets expectation maximization algorithm and applies to systems with axial symmetry. The associated system matrix is calculated off-line, including a model of the  $\gamma$ -event detection in the crystal, taking into account photoelectric effect and Compton scattering interactions. The nonzero elements of the sparse system matrix are stored in disc in an efficient way that allows the fast sequential access to the matrix elements during the reconstruction. A detailed calculation is performed for the voxels corresponding to central plane within the field of view (FOV) of the camera and the remaining values of the system matrix are obtained via translations based on the symmetries of the system along the axial dimension. GATE-based simulations have been used for the validation of the results.

© 2006 Elsevier B.V. All rights reserved.

PACS: 87.58.Fg; 87.57.Gg

Keywords: Image reconstruction; Small animal PET; Monte Carlo simulation; System matrix

## 1. Introduction

Positron emission tomography (PET) is a powerful imaging technique for functional studies with dynamic and quantitative capabilities that are commonly exploited in human clinical research. The challenge for high-resolution small animal PET is to reach the same performance in target volumes that are orders of magnitude smaller than the human size, with good spatial resolution (1 mm or less) and adequate sensitivity. To meet these goals, 3D acquisitions are necessary and suitable image reconstruction methods must be applied.

The max.-likelihood expectation-maximization (MLEM) algorithm [1] and accelerated ordered-subsets implementations (OSEM) [2] are currently widely used in 3D acquisition mode for emission computed tomography, as they produce non-negative images and are especially receptive to model-based compensation for noise degrada-

tion. The MLEM algorithm follows this iterative scheme:

$$x_i^{k+1} = x_i^k \left( \sum_{j=1}^J a_{ij} \right)^{-1} \left[ \sum_{j=1}^J a_{ij} y_j \left( \sum_{i=1}^I x_i a_{ij} \right)^{-1} \right]$$

where at each iteration  $k$  the  $x_i$  image element value (i.e., voxels in 3D images) is updated, being  $y_j$  the acquired projection for the line of response (LOR)  $j$  and  $a_{ij}$  the probability that an event generated in voxel  $i$  is registered in LOR  $j$ . The OSEM algorithm groups the projection data into an ordered sequence of subsets and the standard EM algorithm is applied with a single pass through all subsets. This technique increases the convergence speed by a factor roughly equal to the number of subsets employed [2].

The system matrix (SM)  $\{a_{ij}\}$  can be computed analytically by estimating the volume of overlap of the voxel  $i$  and the volume between the surfaces of the pair of detectors in the LOR  $j$ . These models, however, do not consider other physical effects (e.g., depth-of-interaction, crystal scatter, positron range, non-collinearity of the  $\gamma$ -ray pair, etc.).

\*Corresponding author. Tel.: +34 91 549 57 00x4242;  
fax: +34 91 336 73 23.

E-mail address: [juanen@die.upm.es](mailto:juanen@die.upm.es) (J.E. Ortuño).

Monte Carlo (MC) simulation is an alternative method to the analytic calculation of the SM [3]. This computation can be based on the geometrical configuration of the camera or can further incorporate models of physical processes related to the  $\gamma$ -event generation and detection.

MC simulations for SM calculations have yielded results equally good or even better than analytical approaches in SPECT reconstruction [4]. Fully 3D PET image reconstruction using MC-based precalculated system probability matrix is feasible in small animal PET scanners [5].

The Geant4 application for tomographic emission (GATE) software package [6] is becoming quite popular for PET simulation and is well validated for a wide range of cameras, but the complete tracking of high-energy events along camera and detector response to get sufficient statistics for every  $a_{ij}$  would lead to excessive computation times. Here, GATE has been applied to the generation of synthetic datasets from simulated phantoms and for the validation of the results.

We present here an efficient methodology for the calculation of the SM for 3D-OSEM for high-resolution PET cameras composed of pixelated scintillator crystal blocks, with axial symmetry. The system symmetries have been used to reduce the computational effort, however their use is conditioned by their dependence on the camera's geometry. The SM simulation includes a model of the  $\gamma$ -event detection in the crystal with photoelectric effect and Compton scatter. The SM is stored in disc using sparse matrix format.

## 2. Materials and methods

The proposed SM simulation scheme can be applied to PET scanners with rotating planar detectors [7] composed of pixelated scintillator crystal blocks and shift invariant axial symmetry.

The set of projections is reorganized as a set of oblique sinograms [8] as a function of four variables (Fig. 1): ( $s$ ,  $\varphi$ ,  $\theta$ ,  $r$ ), where  $s$  is the distance between the  $z$  axis and the LOR onto a transaxial plane  $x$ - $y$ ;  $\varphi$  is the azimuthal angle between the LOR and the  $x$  axis;  $\theta$  is the angle between the LOR and the transaxial plane, and  $r$  is the mean between the axial coordinates of the two detector crystals in coincidence ( $z_1$ ,  $z_2$ ). The sinograms are graphically represented on a square grid called Michelogram [9] (Fig. 1) where each dot represents the sinogram associated to a pair of discrete values of ( $\theta$ ,  $r$ ).

Using the parameterization of oblique sinograms for the projected data, each of the elements  $a_{ij}$  of the SM is defined as the probability that an annihilation event, emitted from the volume in the source corresponding to the image element  $i$ , is assigned to a sinogram bin  $j$ . In a pre-calculated SM scheme, the simulation procedure must reproduce the sinogram binning and the interpolation process for each image element. A useful illustration of SM values can include a weighted Michelogram representation

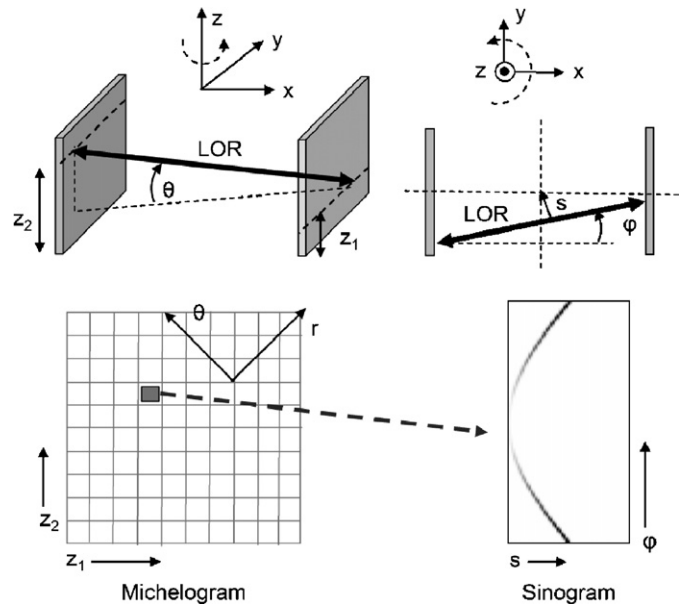


Fig. 1. Projection space representation using Michelograms and sinograms. A LOR between two detectors is assigned to a direct or oblique sinogram (upper left) with  $\varphi$  as azimuthal angle (upper right). Each dot in the Michelogram (down left) represents a direct or oblique sinogram.

where each dot is associated with a grey value representing the total value of the oblique sinogram associated with.

For tomographs with shift invariant axial symmetry, only the voxels of the central slice need to be modeled in detail. The values for the rest of the voxels can be calculated based on parallel axial redundancies and axial symmetry properties [10], providing a reduction factor in storage requirements proportional to the number of rows of pixelated crystals in the axial direction.

The SM is calculated using MC techniques to estimate the probabilities for every sinogram bin. In order to reduce the total calculation time, the simulation is divided in two main steps:

- Simulation of the scanner geometry, which for uniform source distribution and sufficient statistics, is equivalent to an analytical calculation of the intersection volume with the set of tubes of response involved in each sinogram bin [11].
- Simulation of the detector response for incident high-energy  $\gamma$ -rays as a function of the position and angle of incidence.

### 2.1. MC simulation of scanner geometry

The SM simulator uses voxel-based activity distributions placed in the field of view (FOV). The image elements can be point sources, cubic, spherical or cylindrical voxels with or without overlap, and the source distribution can be uniform, or can be represented using Kaiser–Bessel kernels [12].

To reduce the computational requirements, the simulated pairs of  $\gamma$ -rays can be generated uniformly in space and only in directions within the solid angle of coincidence acceptance (that is all emitted  $\gamma$ -rays will be detected). The simulation tracks the rays until their intersection with the detector blocks and eventually assigns a pair of pixelated crystals where the coincidence has been registered and a rotation angle of the detector blocks at the time of the coincidence detection.

## 2.2. MC simulation of detector response

The complete simulation for every  $\gamma$ -ray that intersects the detector surface is replaced by pre-calculated detection probabilities that have been modeled as a function of the angle of incidence and intersection point.

The photon tracking has been modeled using the National Institute of Standard and Technology (NIST) photon cross-section tables [13]. The total cross-section is the sum of the photoelectric, pair production, coherent and incoherent (Compton) scattering, but only Compton and photoelectric effects are significant at 511 keV.

Compton iterations are modeled by sampling the Klein–Nishina distribution. A variation of the Kahn double-rejection technique is used for sampling the scattered photon energy and the scattering angle [14]. The number of allowed scatters and the minimum energy can be limited to speed up the process.

The density of the detected energy distribution is obtained for a set of discretized incident directions and intersection points. The incident energy is constant (511 keV) and the direction is parameterized as a pair of azimuthal and polar angles ( $\varphi_c$ ,  $\theta_c$ ) of the spherical coordinates relative to the planar detector. To obtain the pixelated crystal interaction probabilities, density distributions are integrated over the pixelated crystal volumes. To speed up the process, only the crystals with the  $N$  highest detection probability values are retained in a LUT.

## 3. Results

The proposed simulation scheme has been adapted for an experimental small animal PET scanner [15]. This system has four detector heads, composed of  $35 \times 30$  blocks of  $1.5 \times 1.5 \times 10 \text{ mm}^3$  of LYSO ( $\text{Lu}_{(2-x)}\text{Y}_x\text{SiO}_5:\text{Ce}$ ) crystals. The distance between opposed detectors has been adjusted to 160 mm.

Planar detectors are attached to a gantry with a rotation range of  $180^\circ$ . Only coincidences between opposed heads are allowed. Tomographic image data are acquired in fully 3D mode and binned into  $28^2$  oblique sinograms, with 55 samples in distance  $s$  and 170 angular samples. This projection size maintains the resolution limit calculated for the scanner and crystal dimensions [9]. Nearest-neighbor interpolation is used for binning (one event is assigned only to one sinogram bin).

The photo-fraction values for photoelectric effect and non-coherent scatter for LYSO have been approximated with LSO data loaded from NIST photon cross section tables [13]. The photo-fraction table was downloaded from 50 to 511 keV, with steps of 1 keV.

The crystal MC simulation routine was used to pre-calculate a LUT of  $\theta_c$  values from  $0^\circ$  to  $40^\circ$  (step of  $1^\circ$ ), and  $\varphi_c$  values of  $0^\circ$  to  $360^\circ$  (step of  $3^\circ$ ). The entry point of the incident  $\gamma$ -rays in the pixelated crystal was discretized in  $19 \times 19$  values. One million events were launched for every polar angle  $\theta_c$  obtaining the total deposited energy in each neighboring crystal. The 20 largest neighboring crystal probabilities were stored in the LUT. The total simulation time needed was inferior to 2 h on a PC Pentium 4 platform.

In the SM simulation every event detected is associated with  $20^2$  possible LOR different probabilities, increasing the speed of the process in more than two orders of magnitude with respect to a non-precalculated crystal simulation. The simulated values have been compared with GATE simulation results. The difference is inferior to 0.5%.

### 3.1. System matrix

The results presented in this work have been obtained with the following SM parameters:

- Cubic grid of  $111 \times 111 \times 56$  voxels covering the camera FOV ( $44.8 \times 44.8 \times 44.8 \text{ mm}^3$ ).
- Cubic voxels with uniform distribution, no overlap and size of  $0.4 \times 0.4 \times 0.8 \text{ mm}^3$ . A total number of  $111 \times 111 \times (\pi/4) \approx 9649$  voxels were simulated for the central slice.
- $6 \times 10^5$  initial events/voxel were launched. The total simulation time was approx. 43 h (a mean of 16 s by voxel) in a PC Pentium 4 platform.
- The non-zero elements  $a_{ij}$  ( $i$  in the central slice) were  $1.830 \times 10^9$ . The sparsity of the SM for the central slice was 97.4%.

Using 4 bytes for the position of each matrix element and its value (in sparse storage mode), the pre-calculated 3D SM needs less than 13 GB of hard disc space. The total loading time of this dataset is less than 4 min from an IDE hard disk.

Another SM without crystal simulation was pre-calculated with the same parameters. The sparsity was 99.67%, with a mean of 24290 non-zero values per voxel. Fig. 2 presents a graphical comparison of the result of a single voxel simulation using GATE, the proposed SM, and the simplified SM. The voxel was located 15 mm outside the center of the FOV in the  $x$  direction. The figure shows the logarithm of sum of the sinogram values for every  $z_1$  and  $z_2$ , and weighted Michelograms (the logarithm of the total value of the oblique sinogram of the Michelogram dot is indicated as grey level values).

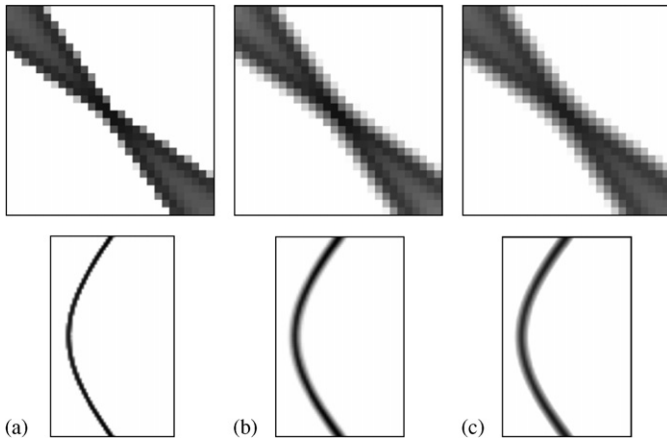


Fig. 2. Different simulations of the SM values associated to a single voxel positioned 15 mm from the centre of the FOV in the central transaxial plane. The weighted michelograms represent the logarithm of the sum of relative probabilities in each oblique sinogram. The histogram of oblique sinograms in  $(\varphi, s)$  is also shown. (a) Simplified simulation, (b) proposed simulation, (c) GATE simulation.

### 3.2. OSEM reconstruction

Fig. 3 shows the result of a reconstruction of a Derenzo-type phantom generated with GATE (2,4, and 8 OSEM iterations, 10 non-overlapping subsets). The phantom was constituted by sets of water-filled rods (diameters of 4.8, 4, 3.2, 2.4, 1.6 and 1.2 mm), with the same distance between surfaces. The rods were surrounded with plastic (polyethylene). Six million coincidence events were collected in the simulation, which included positron range and non-collinearity, scatter and attenuation effects.

The reconstruction time was 40 min/OSEM iteration over all subsets on a single processor Pentium 4 platform. The precalculated matrix values are read twice per iteration. The matrix files were placed in a de-fragmented IDE disk with 56 Mb/s reading speed. The total disc loading time was less than the 20% of the total time of the reconstruction process.

Fig. 4 shows the same phantom reconstructed using a SM, which did not simulate the crystal penetration (taking into account only the scanner’s geometry). It can be seen that the result is noisy. This matrix is sparser and thus the reconstructions times are sorter (only 8 min per OSEM iteration).

The reconstructed phantom data using both the improved and simplified SM were postsmoothed with Gaussian filters. Fig. 5 shows a noise–resolution curve. Noise has been estimated calculating the coefficient of variation (COV) [16] in  $10^3$  voxels of the ROI defined by the rods. The resolution was calculated by blurring the ideal phantom with different Gaussian kernels and matching with the reconstructed image by means of the sum of the square differences (SSD) [17]. With small  $\sigma$  values of the postsmoothing filter, the reconstruction using the improved SM gives better signal/noise ratios.

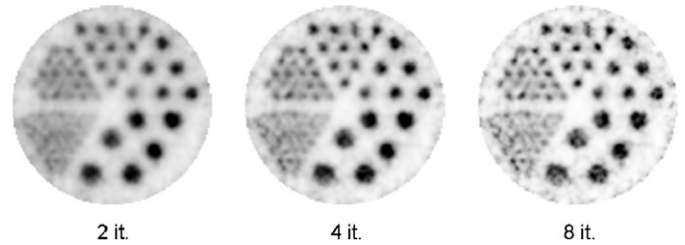


Fig. 3. 3D-OSEM reconstruction of Derenzo-type phantom. Transaxial plane with 2, 4 and 8 OSEM iterations with 10 subsets.

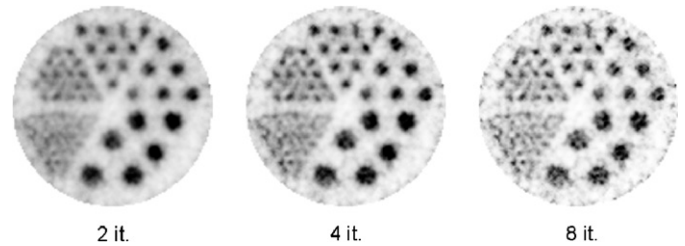


Fig. 4. 3D-OSEM reconstruction of Derenzo-type phantom with simplified SM. Transaxial plane with 2,4 and 8 iterations.

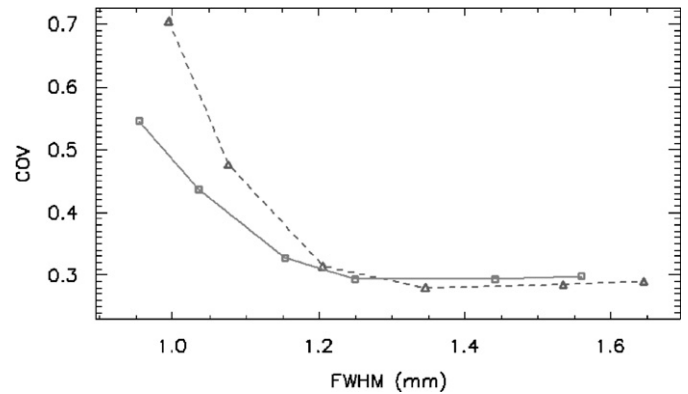


Fig. 5. Noise vs. resolution curve. 3D-OSEM reconstruction of a Derenzo-type phantom (15 iterations and 10 subsets) postsmoothed with different Gaussian filters. The dotted lines represents the curves using the simplified SM in the reconstruction process.

### 4. Conclusions

An efficient method for the calculation of the SM for 3D iterative image reconstruction (IIR) algorithms based on MC techniques has been presented, adapted to a high resolution PET system for laboratory animal imaging. It incorporates the camera’s geometrical configuration and a detailed information on the physical process of the  $\gamma$ -rays interaction in the crystals. Reconstructions of simulated Derenzo phantoms are improved using precalculated detector response data in the SM.

The SM calculation time is less than 2 days in a single PC Pentium 4 and the total hard disk (IDE) loading time is less than 4 min. The IIR time is at least an order of magnitude longer, demonstrating that disk access time is non-critical.

With this methodology it is possible to apply the 3D-OSEM IIR using voxel size smaller than the intrinsic spatial resolution of the camera in a Pentium 4 PC platform.

Future work will include incorporation of further models related to the response of the photomultipliers and the front-end electronics of the system.

### Acknowledgements

This work was partly supported by TEC2004-07052-C02-02, PI041494 and by PI052204.

### References

- [1] L.A. Shepp, et al., IEEE Trans. Med. Imag. 1 (1982) 113.
- [2] H.M. Hudson, et al., IEEE Trans. Med. Imag. 13 (1994) 601.
- [3] G. Kontaxakis, et al., Med. Imag. Biol. 4 (2002) 219.
- [4] D. Lazaro, et al., Nucl. Instr. and Meth. A 527 (2004) 195.
- [5] M. Rafecas, et al., IEEE Trans. Nucl. Sci. NS-51 (2004) 2597.
- [6] G. Santin, et al., IEEE Trans. Nucl. Sci. NS-50 (2003) 1516.
- [7] A.J. Reader, et al., Phys. Med. Biol. 43 (1998) 823.
- [8] M. Defrise, et al., IEEE Trans. Med. Imag. 16 (1997) 145.
- [9] M. Defrise, et al., The Theory and Practice of 3D PET, Kluwer, Dordrecht, 1998 Chapter 2.
- [10] C.A. Johnson, et al., IEEE Trans. Nucl. Sci. NS-42 (1995) 1223.
- [11] E.U. Mumcuoglu, et al., Nucl. Sci. Symp. (1996) 1569.
- [12] R.M. Lewitt, J. Opt. Soc. Am. A 7 (1990) 1834.
- [13] M.J. Berger, et al., NIST Standard Reference Database <<http://physics.nist.gov/PhysRefData/Xcom/Text/XCOM.html>>.
- [14] X.M. Hua, Comput. Phys. 11 (1997) 660.
- [15] J.J. Vaquero, et al., Mol. Imag. Biol. 6 (2004) 102.
- [16] C.A. Johnson, et al., IEEE Trans. Nucl. Sci. NS-44 (1997) 1303.
- [17] M.D.R. Thomas, et al., Phys. Med. Biol. 50 (2005) N187.